

## RESULTS FROM CORE-COLLAPSE SIMULATIONS WITH MULTI-DIMENSIONAL, MULTI-ANGLE NEUTRINO TRANSPORT

TIMOTHY D. BRANDT<sup>1</sup>, ADAM BURROWS<sup>1</sup>, CHRISTIAN D. OTT<sup>2</sup>, AND ELI LIVNE<sup>3</sup>

<sup>1</sup> Department of Astrophysical Sciences, Peyton Hall, Princeton University, Princeton, NJ 08544, USA; tbrandt@astro.princeton.edu, burrows@astro.princeton.edu

<sup>2</sup> Theoretical Astrophysics, Mail Code 350-17, California Institute of Technology, Pasadena, CA, USA; cott@tapir.caltech.edu

<sup>3</sup> Racah Institute of Physics, Hebrew University, Jerusalem, Israel; livne@phys.huji.ac.il

Received 2010 September 23; accepted 2010 November 24; published 2011 January 13

### ABSTRACT

We present new results from the only two-dimensional multi-group, multi-angle calculations of core-collapse supernova evolution. The first set of results from these calculations was published in 2008 by Ott et al. We have followed a nonrotating and a rapidly rotating  $20 M_{\odot}$  model for  $\sim 400$  ms after bounce. We show that the radiation fields vary much less with angle than the matter quantities in the region of net neutrino heating. This happens because most neutrinos are emitted from inner radiative regions and because the specific intensity is an integral over sources from many angles at depth. The latter effect can only be captured by multi-angle transport. We then compute the phase relationship between dipolar oscillations in the shock radius and in matter and radiation quantities throughout the post-shock region. We demonstrate a connection between variations in neutrino flux and the hydrodynamical shock oscillations, and use a variant of the Rayleigh test to estimate the detectability of these neutrino fluctuations in IceCube and Super-Kamiokande. Neglecting flavor oscillations, fluctuations in our nonrotating model would be detectable to  $\sim 10$  kpc in IceCube, and a detailed power spectrum could be measured out to  $\sim 5$  kpc. These distances are considerably lower in our rapidly rotating model or with significant flavor oscillations. Finally, we measure the impact of rapid rotation on detectable neutrino signals. Our rapidly rotating model has strong, species-dependent asymmetries in both its peak neutrino flux and its light curves. The peak flux and decline rate show pole–equator ratios of up to  $\sim 3$  and  $\sim 2$ , respectively.

*Key words:* hydrodynamics – neutrinos – stars: interiors – supernovae: general

*Online-only material:* color figures

### 1. INTRODUCTION

The basic context of a core-collapse supernova is well established: a collapsing, degenerate core releases an enormous amount of energy,  $\sim 1\%$  of which couples to and unbinds the stellar envelope. Despite decades of research, the mechanism of this coupling remains obscure. The collapsing core rebounds at nuclear densities and launches a bounce shock, but detailed simulations in spherical symmetry show that the shock wave stalls at 100–200 km and fails to explode the star (Rampp & Janka 2000; Liebendörfer et al. 2001, 2005; Thompson et al. 2003). The best two-dimensional simulations confirm this result; much of the shock’s energy is lost to nuclear dissociation and escaping neutrinos, and the shock stalls (Bethe 1990; Janka et al. 2007).

The neutrino mechanism, first proposed by Colgate & White (1966) in its prompt form, posits a burst of neutrino emission to energize the shock. In its delayed form (Bethe & Wilson 1985), an imbalance between neutrino absorption and emission behind the shock deposits the additional required energy over several hundred milliseconds. The rate of energy deposition in this “gain region” depends on the relationship between the neutrino flux, which declines as  $\sim r^{-2}$ , and the cooling rate  $\bar{\kappa}acT^4 \sim T^6$ , which generally falls off much more quickly.

Early two-dimensional simulations successfully exploded supernova progenitors by the delayed neutrino mechanism (Herant et al. 1994; Burrows et al. 1995; Janka & Mueller 1996; Fryer & Heger 2000; Fryer & Warren 2002, 2004), though more recent calculations with better neutrino transport generally fail to obtain explosions. An exception is for  $\sim 8\text{--}9 M_{\odot}$  stars, whose steep density gradients reduce the ram pressure of infalling

matter. The post-shock pressure needed to drive an explosion abruptly drops, and a sub-energetic wind-driven supernova follows (Kitaura et al. 2006; Burrows et al. 2007). There are indications that more generic two-dimensional explosions may be obtained with a soft nuclear equation of state, which results in a compact neutron star (Bruenn et al. 2010; Marek & Janka 2009). However, recent experiments (Shlomo et al. 2006) and observations of massive neutron stars (Demorest et al. 2010) favor a stiffer equation of state. Bruenn et al. also find the shock to stall at a much larger radius than other groups, for reasons that are not yet clear. See Nordhaus et al. (2010) and references therein for a more thorough discussion of the state of two-dimensional simulations.

The delayed neutrino mechanism requires  $\sim 10\%$  of the energy emitted by the core in electron and anti-electron neutrinos over the first few hundred milliseconds, a few  $10^{51}$  erg, to be deposited in the post-shock material. The details of this energy deposition depend both on the neutrino–matter coupling and on the hydrodynamics, which determines how long individual particles are subjected to net neutrino heating. This latter point has been shown to be a strong function of dimension, with Murphy & Burrows (2008) and Nordhaus et al. (2010) demonstrating that explosions require  $\sim 30\%$  less neutrino heating in two-dimensional than in one-dimensional, and  $\sim 15\text{--}25\%$  less in three-dimensional than in two-dimensional. Two-dimensional core-collapse simulations display powerful, low-mode oscillations of matter behind the stalled shock as a result of the Standing Accretion Shock Instability (SASI; Foglizzo & Tagger 2000; Blondin et al. 2003; Foglizzo et al. 2007; Iwakami et al. 2008; Yamasaki & Foglizzo 2008; Scheck et al. 2008). Recent three-dimensional calculations confirm the presence of

these oscillations but find their energy to be spread over a wide range of modes forbidden in axisymmetry (Fryer & Young 2007; Fernández 2010; Nordhaus et al. 2010). The coupling of neutrinos to this hydrodynamically unstable matter is central to the supernova problem.

In this work, we present new, hitherto unpublished features of the only two-dimensional multi-group, multi-angle neutrino transport calculations of core-collapse supernova evolution ever performed. Results from these simulations were first published by Ott et al. (2008). These authors studied one nonrotating and one rapidly rotating model, and discussed the overall behavior of the evolution and differences between models evolved using full multi-angle transport and those using multi-group flux-limited diffusion (MGFLD). Ott et al. also studied the angular character of the specific intensity, a quantity that may only be calculated using multi-angle transport. We extend these results, characterizing the spatial variation and coupling of the matter and radiation fields. We also detail the spatial and temporal variations in estimated neutrino signals observable from Earth. We obtain similar results to Marek et al. (2009) and Lund et al. (2010), but with more detailed neutrino transport and a different statistical technique.

Ott et al. (2008) demonstrated that multi-angle transport self-consistently captures the transition from diffusion to free-streaming, eliminating flux-limiter artifacts (though introducing artifacts intrinsic to  $S_n$  in the optically thin limit; see Castor 2004). They also showed that the net neutrino heating rates behind the stalled shock are higher in their nonrotating model with multi-angle transport than with flux-limited diffusion. Though the difference ranges from  $\sim 5\%$ – $10\%$  at early times to  $\sim 20\%$ – $30\%$  at later times, Ott et al. do not find their two-dimensional multi-angle model to be significantly closer to explosion.

This paper complements Ott et al. (2008) by examining in detail the coupling between matter and radiation and the relationship between spatial and temporal fluctuations in hydrodynamic quantities and neutrino spectral energy densities. We find that the magnitude of fluctuations is substantially lower in the radiation fields than in the local matter in the critical region behind the stalled shock. This results both from the more quiescent hydrodynamics in the regions where the neutrinos were predominantly emitted and from the multi-angle character of the specific intensity. Because the local radiation field is an integral over contributions from many sources at depth, fluctuations tend to be smoothed out. This is an important effect that radial, “ray-by-ray” transport methods neglect.

We also extend Ott et al. (2008) to investigate the relationship between variations in the hydrodynamics at depth and observable variations in the neutrino signal. Following the calculations of Marek et al. (2009) and the detailed post-processing of Lund et al. (2010), we then estimate the detectability of these rapid neutrino fluctuations in the water Cherenkov detectors IceCube and Super-Kamiokande (Super-K). We find that fluctuations characteristic of convective overturn and shock oscillations could be observed in our nonrotating model, but are very weak for our rapidly rotating progenitor. Finally, we calculate the effects of rotation on the anisotropy of the observed neutrino signal. We confirm the basic effects of rotation detailed in Walder et al. (2005), whereby centrifugal support suppresses radiation in the equatorial plane. We also detail the evolution of the pole–equator anisotropy and calculate the probability distribution of observable fluxes.

The paper is organized as follows. In Section 2, we describe our numerical techniques and pre-collapse models. In Section 3, we present the spatial variation of matter and radiation fields, highlighting the spatial uniformity of radiation due to the location of the decoupling region and the multi-angle character of the specific intensity. In Section 4, we discuss temporal oscillations of matter and radiation, and present the phasing of dipolar oscillations in these quantities with the shock position. Having established a connection between hydrodynamic oscillations and neutrino fluctuations, we estimate the detectability of these fluctuations in Section 5. In Section 6, we address the impact of rapid rotation on the detectable signal, finding an orientation-dependent flux asymmetry of up to a factor of  $\sim 3$  at early times and light curves that strongly depend on both species and viewing angle. We conclude in Section 7.

## 2. METHODS

The numerical methods and initial models used in this work are described in detail in Ott et al. (2008) and references therein. In this section, we summarize the important points and refer the reader to these references for a more thorough discussion.

### 2.1. Hydrodynamics

We use the radiation-hydrodynamics code VULCAN-2D, described by Livne et al. (2004) and Burrows et al. (2007). The hydrodynamics module solves the Newtonian Euler equations with artificial viscosity in two steps: a Lagrangian step followed by a remapping onto an arbitrary axisymmetric grid. We use a polar grid with 120 polar angles and 230 logarithmically spaced radial zones from 20 to 4000 km. To avoid small cells (and prohibitive time step restrictions), we transition to a pseudo-Cartesian grid in the inner 20 km. We implement Newtonian gravity with a grid-based Poisson solver, and we use the finite-temperature nuclear equation of state of Shen et al. (1998a); Shen et al. (1998b).

### 2.2. Radiative Transfer

VULCAN-2D includes two radiative transfer modules: MGFLD and a discrete ordinates Boltzmann solver ( $S_n$ ). Flux-limited diffusion solves the equations of radiative transfer in the diffusion approximation, using a flux-limiter to handle the transition to free-streaming. The  $S_n$  solver discretizes the polar and azimuthal angles  $\theta$  and  $\phi$  of the specific intensity, preserving its multi-angle character. It includes emission, absorption, and isotropic scattering with the transport cross section  $\sigma^s$ , related to the total cross section  $\sigma_T^s$  by  $\sigma^s \equiv (1 - \langle \cos \theta \rangle) \sigma_T^s$ , but neglects  $O(v/c)$  terms, including Doppler shifts and neutrino advection. We use a constant spacing in  $\cos \theta$  and a variable number of azimuthal angles  $\phi$  to tile the sphere as uniformly as possible. With eight polar angles ( $S_8$ ), we use a total of 40 ( $\theta, \phi$ ) pairs, while  $S_{12}$  uses 92 and  $S_{16}$  uses 162 pairs. These angles are the possible directions of the specific intensity and, thus, of radiation transport.

For this study, we have employed a hybrid of MGFLD and  $S_n$ , as discussed in Ott et al. (2008). We collapse our progenitor models and follow them after bounce for the ensuing 160 ms using MGFLD. We then transition to  $S_n$  by freezing the hydrodynamics long enough to allow the radiation to reach equilibrium with the matter. We continue to use MGFLD in the inner 20 km, where the matter is optically thick to all species and energy groups and the diffusion approximation is accurate. We then restart the hydrodynamics and follow the evolution

of the core using this hybrid approach, with MGFLD deep in the core and  $S_n$  at radii greater than 20 km. Because the computational cost of  $S_n$  scales as  $n^2$ , we are only able to run the full evolutionary calculations with eight polar angles. We have used  $S_{16}$  to compute snapshots of the radiation field at 160 ms after bounce.

We perform all radiation transport with three neutrino species and sixteen energy groups. The first energy group is at 2.5 MeV, and the rest are logarithmically spaced from 5 to 220 MeV. While all neutrinos participate in neutral current reactions, only  $\nu_e$  and  $\bar{\nu}_e$  are subject to charged-current interactions. Because of their similar (neutral-current) cross sections, we group  $\nu_\mu$ ,  $\bar{\nu}_\mu$ ,  $\nu_\tau$ , and  $\bar{\nu}_\tau$  into a single “species,” which we designate “ $\nu_\mu$ .”

### 2.3. Progenitor Models

We begin our calculations with two  $20 M_\odot$  pre-collapse models of Woosley et al. (2002). To study the effects of rapid rotation, we apply an angular velocity profile to one of our models of the form

$$\Omega(R) = \Omega_0 \frac{1}{1 + (R/A)^2}, \quad (1)$$

where  $R$  is the cylindrical radius,  $A$  sets the scale of differential rotation, and  $\Omega_0$  is the central angular frequency. Because of the computational cost of  $S_n$ , we are unable to run a set of models to explore  $A$ – $\Omega_0$  space. Instead, we study the effects of very rapid rotation using  $A = 1000$  km and  $\Omega_0 = \pi$  rad s<sup>−1</sup>, corresponding to an initial central period of 2 s. This central period is faster than those currently favored for evolved massive stars (Maeder & Meynet 2000; Heger et al. 2005). An important exception is for collapsar models, which require very fast pre-collapse stellar rotation rates of  $\lesssim 5$  s in the core (Woosley 1993). Without angular momentum loss, our rotation rate would result in a “millisecond-period” protoneutron star, significantly faster than estimated pulsar birth spin rates (Emmering & Chevalier 1989; Faucher-Giguère & Kaspi 2006; Ott et al. 2006). Our two models therefore bracket the spin range of plausible progenitors.

## 3. RESULTS: ANGULAR VARIATIONS IN RADIATION AND HYDRODYNAMICS

There is good evidence that it is easier to explode a supernova by the delayed neutrino mechanism in two dimensions than in one (Murphy & Burrows 2008). The extra dimension opens a rich array of instabilities, increasing the residence time of particles in the gain region where they undergo net neutrino heating (Murphy & Burrows 2008). Nordhaus et al. (2010) have recently extended this result to three dimensions, showing that a three-dimensional explosion requires  $\sim 15\%$ – $25\%$  less neutrino luminosity than its two-dimensional analog. The central importance of neutrino heating in multiple dimensions highlights the need to accurately capture the coupling between matter and radiation in the semi-transparent gain region, over which the neutrino optical depths range from a few hundredths to a few tenths.

Radiative transfer in the core-collapse supernova context is fundamentally a seven-dimensional problem, with six dimensions of phase space and one of time. In addition, there are six neutrino species (three particles and their antiparticles). Because the neutrinos are not in thermal equilibrium with their surroundings, simple approximations to full Boltzmann transport may miss important physical effects. The most obvious example is the phenomenon of net neutrino heating, which occurs

predominantly because the ambient radiation field in the region behind the stalled shock is much harder than it would be in local thermodynamic equilibrium. In this section, we present results from our nonrotating model, demonstrating the striking spatial uniformity of radiation relative to the matter fields throughout the gain region. The radiation fields in our rotating model vary smoothly from pole to equator. Because the rapid rotation inhibits convection so strongly, there is little small-scale variation in either the radiation or the hydrodynamics.

### 3.1. Variation of Neutrino and Matter Fields with Angle

The post-shock region of a core-collapse supernova displays a range of hydrodynamic phenomena, from large-scale shock oscillations and convective overturn to smaller scale turbulence. While these phenomena directly influence the local properties of matter, their effects on neutrinos are more subtle and depend on the strength of the coupling between matter and radiation. In the optically thick core, the diffusion limit obtains, and radiation and matter are in local thermodynamic equilibrium. In the free-streaming limit, the neutrino properties largely reflect those of matter near the appropriate neutrinospheres where they are emitted. We define the neutrinospheres to be the (energy- and species-dependent) radii  $r_\tau$ , where the radial optical depths equal  $2/3$ :

$$\int_{r_\tau}^{\infty} \langle \kappa(r, \theta) \rho(r, \theta) \rangle_\Omega dr = \frac{2}{3}. \quad (2)$$

Because of the rapid transition to free-streaming, the above picture suggests two relatively distinct regimes. The angular distribution of radiation should resemble that of the local matter only where the material is optically thick.

We present the angular dependence of hydrodynamic and radiation quantities in Figure 1 at radii of 50 km and 100 km at three epochs after bounce in our nonrotating model. These plots clearly indicate the distinction between the two regimes discussed above; only the top left panel shows a region where neutrino spectral energy densities (indicated at representative energies by dot-dashed lines) resemble the angular distribution of density  $\rho$  and electron fraction  $Y_e$ . All quantities are plotted at fixed radius and normalized to their average values over  $4\pi$  sr. The neutrino energies used are the rms values for each species at large radius:

$$\varepsilon_{\text{rms}} = \sqrt{\langle \varepsilon^2 \rangle} \equiv \left( \frac{\int \varepsilon^2 F_\nu(\varepsilon) d\varepsilon}{\int F_\nu(\varepsilon) d\varepsilon} \right)^{1/2}, \quad (3)$$

where  $F_\nu(\varepsilon)$  is the neutrino energy flux spectrum. These rms energies increase with time (see Ott et al. 2008, Figure 18). We use the energy groups closest to the rms values over the first few hundred milliseconds after bounce: 16, 21, and 27 MeV for  $\nu_e$ ,  $\bar{\nu}_e$ , and “ $\nu_\mu$ ,” respectively. Because the “ $\nu_\mu$ ” couple to matter more weakly than electron and anti-electron types, their neutrinospheres lie deeper in the protoneutron star core. The “ $\nu_\mu$ ” spectra are therefore harder, reflecting the higher temperatures that prevail where they are emitted.

As the core evolves during the postbounce phase, variations with angle increase in all quantities and at all radii. This is due to two effects: (1) growth in the vigor of convective overturn and large-scale shock oscillations, and (2) the contraction of the protoneutron star, so that a fixed radius moves outward in Lagrangian coordinates. The effects of contraction are most clearly seen at a radius of 50 km between 160 ms (top left panel of Figure 1) and 250 ms after bounce (top center panel). At

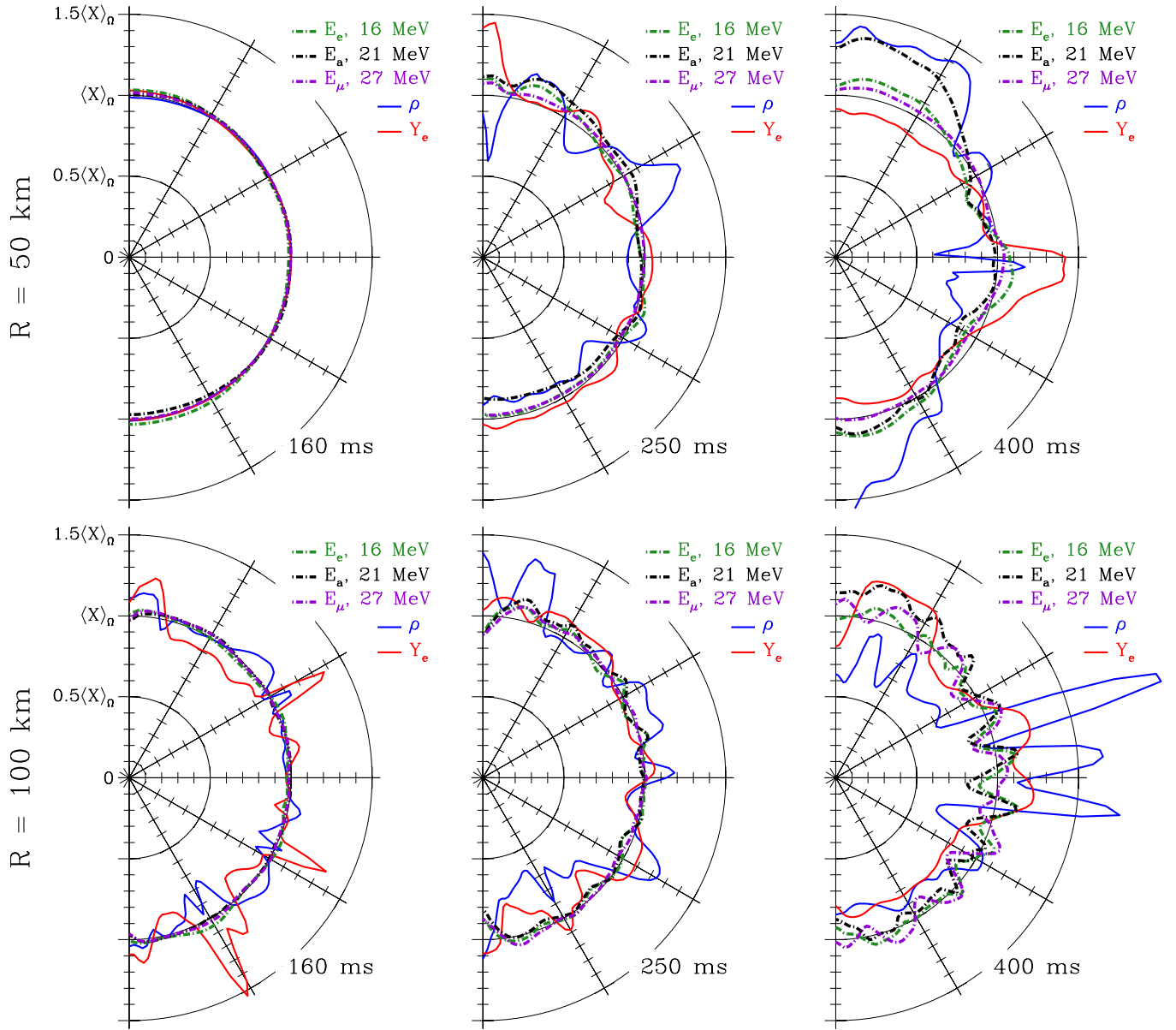


**Figure 1.** Polar plots showing the values of  $\rho$ ,  $Y_e$ , and the spectral energy density of each species near its rms energy ( $\sqrt{\langle \epsilon_v^2 \rangle}$ , Equation (3)), for the nonrotating model.  $E_e$ ,  $E_a$ , and  $E_\mu$  denote electron, anti-electron, and mu/tau neutrino types, respectively. The radial coordinate is proportional to each value of the quantity at a fixed physical radius, 50 km in the upper plots and 100 km in the lower plots, normalized to its average over  $4\pi$  sr. The matter and radiation fields both show more variation with angle at late times, as the shock oscillations grow in amplitude. However, the neutrino energy densities always vary less with angle than the thermodynamic quantities  $\rho$  and  $Y_e$ .

(A color version of this figure is available in the online journal.)

160 ms, the base of the convective zone lies at about 70 km radius, and the top left panel displays the properties of a radiative zone. By 250 ms after bounce, the base of the convective zone has sunk to around 45 km. The region sampled by the top center panel is therefore convectively unstable. As a result, fractional fluctuations in  $\rho$  and  $Y_e$  increase from  $<1\%$  at 50 km and 160 ms after bounce to about 10% at the same radius at 250 ms.

While  $\rho$  and  $Y_e$  vary strongly with angle in the convective regions, up to a factor of  $\sim 2$  at late times (see bottom right panel of Figure 1), variations in neutrino energy densities remain smaller throughout the gain region. Even at 400 ms after bounce at 100 km (lower right panel), where the variation in density reaches a factor of two, fractional variations in neutrino energy densities remain  $\lesssim 20\%$ . These neutrinos are predominately emitted by matter beneath the base of the convective zone, and

retain the relatively smooth angular distribution characteristic of that region. As discussed in the following section, their angular distribution also becomes smoother with increasing radius due to the integrated contributions from sources at many angles. This effect can only be properly captured by full, multi-angle neutrino transport.

### 3.2. Radial Dependence of Neutrino and Matter Variation

Figure 1 indicates a sharp distinction between the angular dependence of matter in radiative and convective zones. To examine the radial dependence of angular variations, we introduce the fractional angular variance, defined for a quantity  $X$  as

$$\sigma_X^2(r, t) \equiv \frac{\langle X^2(r, t) \rangle_\Omega}{\langle X(r, t) \rangle_\Omega^2} - 1, \quad (4)$$

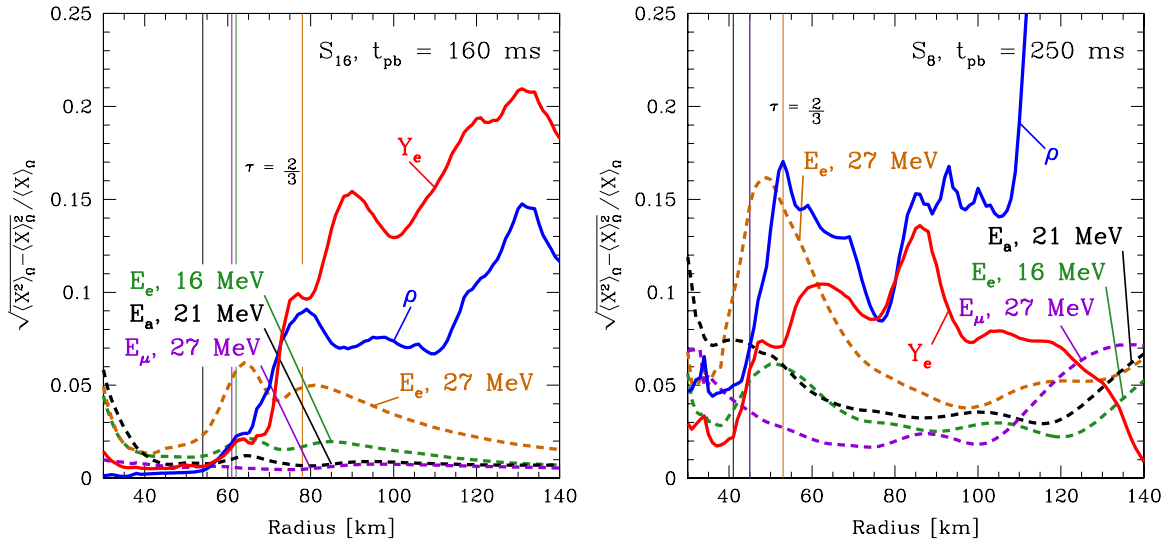


**Figure 2.** Normalized angular deviation  $\sqrt{\langle X^2 \rangle_\Omega - \langle X \rangle_\Omega^2} / \langle X \rangle_\Omega$  in a quantity  $X$ , Equation (4), as a function of radius. Here,  $\nu_e$  represents the spectral energy density  $E_i$  of  $\nu_e$ ,  $E_a$  of  $\bar{\nu}_e$ , and  $E_\mu$  of “ $\nu_\mu$ .” Deviations in  $\rho$  and  $Y_e$  increase sharply at the base of the convective zone and remain high throughout the gain region. Deviations in neutrino energy densities decrease beyond the neutrinospheres (denoted by thin vertical lines) due to the integrated contribution of sources from many angles at depth. Throughout the convective region, angular deviations of energy density in all but the highest energy  $\nu_e$  are much lower than deviations in  $\rho$  and  $Y_e$ . The neutrino energies shown, except 27 MeV for  $\nu_e$ , are each species’ approximate rms energy ( $\sqrt{\langle \epsilon^2 \rangle}$ , Equation (3)). Increases in the angular deviations of  $E_i$  at large radius are banding artifacts of the discrete angles used in  $S_n$ .

(A color version of this figure is available in the online journal.)

where  $\langle X \rangle_\Omega$  denotes the average value of  $X$  over  $4\pi$  sr. With this definition,  $\sigma_X^2 = 0$  if and only if the quantity  $X$  is uniform in angle. The fractional angular deviation,  $\sigma_X$ , is then  $\sqrt{\sigma_X^2}$ .

Figure 2 shows the fractional angular deviation of the same quantities plotted in Figure 1 at 160 ms and 250 ms after bounce for our nonrotating model. The hydrodynamic variables  $\rho$  and  $Y_e$  clearly show the base of the convective zone, which sinks from  $\sim 70$  km at 160 ms to  $\sim 45$  km at 250 ms after bounce. The neutrino spectral energy densities are relatively uniform throughout the gain region, as suggested by Figure 1. This is especially striking at 160 ms after bounce (left panel), which was computed with 16 polar angles for neutrino transport. This snapshot shows increasing angular variation in the neutrino fields up until roughly the appropriate neutrinospheres (Equation (2)), and then a transition to a regime where the radiation becomes more spatially uniform with radius. This is especially apparent in high energy electron neutrinos (like the 27 MeV energy group shown here). Because of the  $\sim \epsilon^2$  dependence of neutrino cross sections, higher energy neutrinos have neutrinospheres at larger radii, where the matter begins to convect. After the radiation decouples, however, multi-angle effects smooth its angular distribution.

Neutrinos in the model at 250 ms after bounce have the same behavior, first showing more variation with angle and finally becoming smoother past the neutrinospheres. However, because only eight polar angles were used for neutrino transport,  $S_n$  artifacts begin to appear at  $\sim 100$ – $150$  km in radius. In  $S_n$ , neutrinos can only be transported along the  $n$  discrete polar angles defined in the solver. In regions of low optical depth, this tends to confine radiation to radial rays, as discussed in, e.g., Castor (2004) and Livne et al. (2004).

The radiation field tends to become more uniform with angle because of the multi-angle character of the specific intensity; its value at a point is an integral over contributions from many sources (and therefore many angles) at depth. Because an observer at large radius can effectively “see” emission from

**Table 1**  
Angular Deviation in  $\nu_e$  Spectral Energy Density

$\epsilon_\nu$ (MeV)	$r_\tau$ (km)	$\sigma(r_\tau)^a$	$\sigma(150 \text{ km})^b$
16	62	0.020	0.0068
21	69	0.029	0.0096
27	78	0.049	0.014
35	91	0.074	0.022

**Notes.**

<sup>a</sup> Fractional angular deviation in spectral energy density (Equation (4)) at the appropriate neutrinosphere (Equation (2)).

<sup>b</sup> Fractional angular deviation in spectral energy density (Equation (4)) at 150 km.

an entire hemisphere, variations in the properties of radiation near the neutrinospheres tend to average out. As a result, the illumination of matter in the gain region is more uniform than would be inferred with purely radial transport. We quantify this effect in Table 1, comparing the fractional angular deviation for neutrino energy densities at their neutrinospheres to that at 150 km in our nonrotating  $S_{16}$  snapshot. Table 1 demonstrates that the fractional angular deviation is a decreasing function of radius, as discussed above, but an increasing function of neutrino energy. Because higher energy neutrinos decouple at larger radii, they interact more with convecting matter. However, multi-angle effects smooth out much of this variation. In our  $S_{16}$  snapshot, fractional variations in  $\rho$  and  $Y_e$  are  $\sim 10\%$ – $20\%$  throughout the convective zone, while fractional variations in the neutrino spectral energy densities fall to  $\lesssim 2\%$  by 150 km.

Many groups currently use “ray-by-ray” radial transport<sup>4</sup> because of its considerably lower cost (e.g., Buras et al. 2006; Marek & Janka 2009; Bruenn et al. 2010). The “ray-by-ray plus” method (Buras et al. 2006) performs accurate lateral transport in optically thick regions by keeping terms associated with lateral neutrino advection and pressure gradients. However,

<sup>4</sup> First introduced into supernova theory by Burrows et al. (1995).

this technique omits the angular flux terms, which transport neutrinos relative to the gas, and may therefore exaggerate the anisotropy of the neutrino distribution at large radius (see Section 2.3.2 of Buras et al. 2006). Our results with full multi-angle transport provide a baseline, which could be used to calibrate an otherwise ad hoc coupling of neighboring rays in semitransparent regions. Such an approach might provide more accurate transport at a minimal additional cost over current “ray-by-ray” methods.

#### 4. THE RELATIONSHIP OF NEUTRINOS TO SHOCK OSCILLATIONS

The most visually striking feature of two-dimensional core-collapse simulations is the large-scale oscillation of matter behind the stalled shock. In our nonrotating model, the shock position has a strong dipolar component that oscillates at  $\sim 50$  Hz. In our rapidly rotating model, the oscillations are much weaker and emerge several hundred milliseconds later. The relationship between the shock position and oscillations in the post-shock material is complex and has been discussed at length in Foglizzo & Tagger (2000), Blondin et al. (2003), and Foglizzo et al. (2007). Here, we compute the phasing of oscillations in hydrodynamic and radiation quantities as a function of radius, tracing the response of matter and radiation throughout the post-shock region. We thus establish the temporal relationship of the observable neutrino emission to the unobservable hydrodynamics in the core.

We seek to isolate the strongest oscillatory components of the shock radius and post-shock hydrodynamic and radiation quantities. Because these oscillations are dominated by low- $l$  (in particular  $l = 1$ ) modes in two-dimensional, we use the dipole moments of all quantities. We define these to be the  $l = 1$  spherical harmonic coefficients in axisymmetry ( $m = 0$ ),

$$a_1(X(r)) \equiv \frac{\sqrt{3}}{2} \int_0^{2\pi} d\phi \int_0^\pi X(r, \theta) \cos \theta \sin \theta d\theta, \quad (5)$$

in a quantity  $X$ . We also define the normalized cross-correlation function between two quantities  $X$  and  $Y$  with temporal offset  $\tau$  as

$$C(X, Y, \tau) \equiv \frac{\int dt [X(t) - \langle X \rangle][Y(t - \tau) - \langle Y \rangle]}{\sigma_X \sigma_Y \Delta t}. \quad (6)$$

Here,  $\langle X \rangle$  denotes the temporal average of  $X$ , and  $\sigma_X$  its standard deviation. Thus,  $C(X, X, 0)$  is the normalized autocorrelation with zero offset and equals unity, while a negative value of  $C$  indicates an anticorrelation. We define the delay between  $X$  and  $Y$  to be the offset  $\tau$  that maximizes their cross-correlation function. We then convert this delay into a phase difference using a periodicity of 19.4 ms. This is the period of the autocorrelation function of the shock position,  $C(R_{\text{sh}}, R_{\text{sh}}, \tau)$ , and represents an average SASI frequency in our nonrotating model. In the following analysis, we use the dipole coefficients  $a_1$  of radiation and hydrodynamic quantities as the inputs to Equation (6).

In Figure 3, we show the phase differences between  $a_1(R_{\text{sh}})$  and the dipole components of hydrodynamic and radiation quantities in our nonrotating model. The vertical axis is the phase in degrees by which  $a_1(R_{\text{sh}})$  lags a given quantity, while the line thickness corresponds to the maximum magnitude of the cross-correlation function, with thicker lines indicating stronger correlations. The hydrodynamic quantities show gradual phase shifts throughout the post-shock region, while the radiation

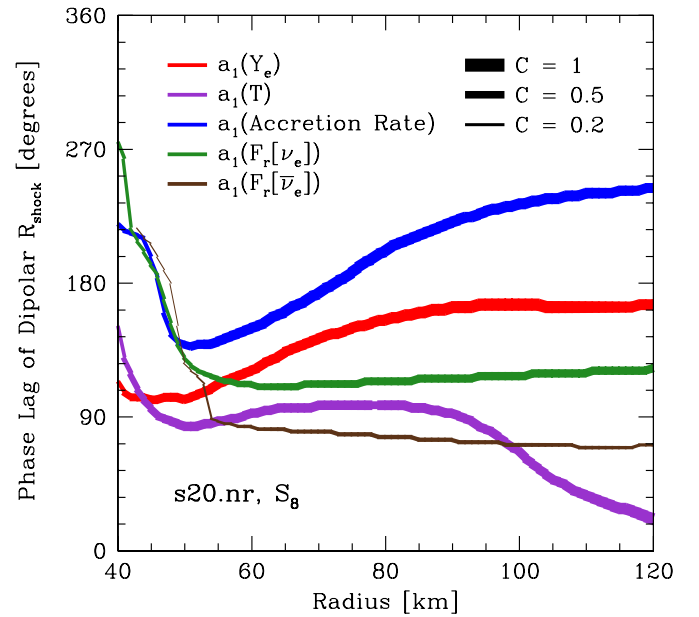


**Figure 3.** Phase (in degrees) by which the dipole component  $a_1$  of the shock position (Equation (5)) lags dipolar radiation and hydrodynamic quantities. The line thicknesses are proportional to the values of the normalized cross-correlation, with thicker lines indicating closer relationships. The phase lag between the shock position and the mass accretion rate and  $Y_e$  gradually decreases, reflecting the fact that the post-shock region is not moving as a solid body. Temperature responds to compression and expansion; its maximum asymmetry occurs when the shock position is most symmetric (and its velocity is least symmetric). The phasing of neutrino emission is determined near a radius of 50 km, and its correlation with the shock position is largest in  $\nu_e$ . Electron neutrinos have the most emission in convective regions and the strongest link to turbulent hydrodynamics.

(A color version of this figure is available in the online journal.)

quantities display a constant phase past their decoupling radii. These phase shifts may be thought of as sonic delays, reflecting the fact that the post-shock material is not moving as a solid body.

The phase shifts of individual hydrodynamic quantities provide insights into the dynamics of the post-shock material. The accretion rate is closely related to the velocity, and its dipole component is slightly more than  $90^\circ$  out of phase with that of the shock position. At the shock radius itself, the phase difference would be exactly  $90^\circ$ , as with a simple harmonic oscillator. The phase lag varies with depth due to the finite sound speed, reaching an offset of  $180^\circ$  near 70 km. This delay is also illustrated by the advected quantity  $Y_e$ . At large radius, the electron fraction peaks on the side opposite to that of the shock position due to the expansion of deleptonized material. The peak temperature asymmetry at depth leads the maximum extent of the shock by  $\sim 90^\circ$ . At large radius, the temperature asymmetry reflects the shock asymmetry, as the hot post-shock material expands into unshocked infalling matter. We have not shown the total heating rate integrated over the gain region, which is primarily a function of the volume of the gain region. Its dipole moment is almost perfectly in phase with that of the shock radius.

Shock oscillations are hydrodynamic phenomena, and the relationship of the shock asymmetries to the radiation field is weaker than that to hydrodynamic quantities. As shown in Figure 3, however, a clear correlation between the shock radius and neutrino asymmetries is present, particularly in electron neutrinos. The phasing of this relationship is determined near 50 km, and is largely due to the minority of electron neutrinos

emitted from convective regions. Anti-electron neutrinos, which decouple almost entirely at greater depth, display a weaker cross-correlation with dipolar asymmetries in the shock radius. The asymmetry in both species' asymptotic flux is nearly in phase with matter outflows at large radius, and leads the asymmetry in the shock position by about  $70^\circ$  ( $\bar{\nu}_e$ ) and  $120^\circ$  ( $\nu_e$ ). Though the fractional asymmetries are lower in radiation than in hydrodynamic quantities, Figure 3 demonstrates that large-scale oscillations are largely responsible for the asymmetries that we do observe. A detection of neutrino fluctuations in a real supernova would provide strong evidence for shock oscillations.

## 5. DETECTABILITY OF RAPID NEUTRINO FLUCTUATIONS

In the previous section, we showed that large-scale oscillations of matter behind the stalled shock are correlated with oscillations in neutrino flux, particularly in  $\nu_e$ 's. The detectability of these rapid neutrino fluctuations depends on the fraction of neutrinos emitted from convective regions and on the vigor of large-scale overturn and global oscillations. The fluctuations must be sufficiently large to be distinguishable from shot noise in a smoothly declining signal. Large-scale hydrodynamic oscillations impose a periodicity on these fluctuations, opening up a variety of observational tests. In this section, we examine the prospects for detecting rapid fluctuations in the emission of a real supernova. A robust detection of periodicity in the neutrino signal might confirm the large-scale oscillations predicted by two-dimensional core-collapse simulations.

### 5.1. Estimating the Signal

The neutrino signal detected on Earth is the product of the spectral flux and the detector response function. For a nearby supernova, the best counting statistics will be provided by IceCube and Super-K, both water Cherenkov detectors primarily sensitive to anti-electron neutrinos. Each has a response approximately proportional to the square of the neutrino energy, so that the

$$\text{“signal”} \propto \int_0^\infty f_\varepsilon(\theta, R, t) \varepsilon^2 d\varepsilon, \quad (7)$$

where the number flux  $f$  is a function of viewing angle  $\theta$ , supernova distance  $R$ , and time. The constant of proportionality depends on the fiducial volume of the detector, 22.5 kt for Super-K (Ikeda et al. 2007) and 940 kt for IceCube (Kowarik et al. 2009). Super-K has almost no background, while IceCube will have an estimated background rate of approximately  $1.34 \times 10^3 \text{ (ms)}^{-1}$  (Kowarik et al. 2009). Designed for exceptionally energetic neutrinos, IceCube would be unable to resolve individual neutrino energies or trajectories, but would observe a supernova burst as an increase above its normal background. Super-K has a negligible background and would provide approximate neutrino directions and energies, but with far fewer events. These two detectors also have different temporal resolutions. IceCube bins its data into intervals of 1.6384 ms (Kowarik et al. 2009), while Super-K resolves the relative arrival time of individual events to microseconds (Ikeda et al. 2007).

In Figure 4, we show estimated signals computed by Equation (7) for both our nonrotating and our rapidly rotating models. The fractional fluctuations in electron and anti-electron estimated signals are  $\sim 10\%$  in the nonrotating model and are weak functions of viewing angle. The magnitude of these fluctuations is much larger than the secular change of the signal over a SASI period. In contrast, the estimated signal for our

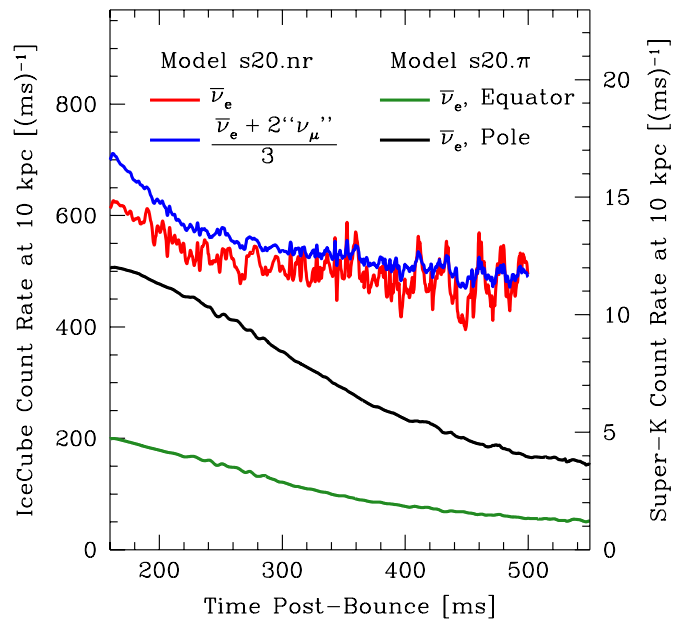


**Figure 4.** Estimated  $\bar{\nu}_e$  signals (Equation (7)) and fully mixed signals  $1/3 \bar{\nu}_e + 2/3 \nu_\mu$  of our nonrotating model and  $\bar{\nu}_e$  “signals” of our rapidly rotating model. The fractional fluctuations are as high as 10% in the nonrotating model, but  $\lesssim 2\%$  in the rotating case. To the extent that neutrino flavor mixing does occur, smoothly declining “ $\nu_\mu$ ” will dilute the rapid fluctuations shown here in  $\bar{\nu}_e$ .

(A color version of this figure is available in the online journal.)

rotating model is dominated by smoothly declining accretion luminosity and cooling. Rapid rotation stabilizes the post-shock region against convection and suppresses oscillations in the hydrodynamics and neutrinos. While these “signals” do display some periodic modulation, the magnitude of rapid fluctuations is comparable to the secular change over a period. Orientation effects, which we explore in detail in Section 6, dominate in our rapidly rotating model.

The rapid variations in our neutrino “signals” arise from a combination of vigorous convection, modulated by the SASI, and neutrino emission from the convecting region. If the power in shock oscillations is spread over a wider range of modes (as has been suggested by recent three-dimensional simulations), these oscillations might leave a weaker imprint on the neutrinos. Such a possibility needs to be addressed quantitatively, ideally with full three-dimensional simulations. Sophisticated post-processing of three-dimensional hydrodynamic calculations, like those of Nordhaus et al. (2010), may also provide insight.

We also caution that our estimated “signals” neglect neutrino flavor oscillations. Because they decouple from matter beneath the convective layer, “ $\nu_\mu$ ” show fractional fluctuations of  $\lesssim 1\%$  even in our nonrotating model. Flavor mixing would make it more difficult to detect rapid neutrino fluctuations by diluting the  $\bar{\nu}_e$  with these “ $\nu_\mu$ .” Lund et al. (2010) found that under an assumption of complete, energy-independent mixing of all species, fractional fluctuations in their estimated “signals” declined by  $\sim (2/3)$ . We also show detection results for this extreme case in order to bracket the range of physically plausible neutrino signatures of flux variations, and find similar results.

### 5.2. Detecting the Fluctuations

The estimated neutrino signals shown in Figure 4 are each a superposition of a smoothly declining component and a smaller, rapidly varying component correlated with the hydrodynamics around the protoneutron star. Here, we estimate the maximum

distance to our nonrotating supernova model at which these variations would be detectable by IceCube and Super-K. Lund et al. (2010) estimated the detectability of rapid fluctuations in their models using high-frequency Fourier components. They found that, neglecting flavor oscillations, IceCube would be able to detect a few high-frequency components in their model at 10 kpc. Here, we use the Rayleigh test (Leahy et al. 1983), a different and simpler method common in radio and X-ray astronomy, and obtain similar results.

The Rayleigh test is a test for periodicity in a discrete time series. Given an assumed period, each element of the series is assigned a phase  $\phi$  and thus a unit vector in  $r$ - $\phi$  space. The Rayleigh statistic  $\mathcal{R}$  is the normalized magnitude of the vector sum of these elements,

$$\mathcal{R} = \frac{2}{N} \left[ \left( \sum_{i=1}^N \sin \phi_i \right)^2 + \left( \sum_{i=1}^N \cos \phi_i \right)^2 \right], \quad (8)$$

over a temporal range consisting of an integer number of periods. For a constant signal with only Poisson noise,  $\mathcal{R}$  will be drawn from a  $\chi^2$  distribution with two degrees of freedom (Leahy et al. 1983).

The Rayleigh test, as described above, takes its null hypothesis to be a uniform signal. In the case of supernova neutrino emission, we wish to extend the null hypothesis to include a smoothly, secularly changing signal (but still without rapid fluctuations). We may accomplish this with a slight modification to the Rayleigh test. In addition to the phase angle  $\phi$ , we define a second phase angle  $\theta \equiv \phi + \pi$ . We take our temporal range for  $\theta$  to be an integer number of periods, but with its starting and ending times offset by one-half period from their values with  $\phi$ . In essence, we use the difference between the first and last half-periods to calibrate out any secular change. We then define our modified Rayleigh statistic  $\mathcal{R}'$  to be

$$\mathcal{R}' = \frac{4}{N_\phi + N_\theta} \left[ \frac{1}{4} \left( \sum_{i=1}^{N_\phi} \sin \phi_i - \sum_{j=1}^{N_\theta} \sin \theta_j \right)^2 + \frac{1}{4} \left( \sum_{i=1}^{N_\phi} \cos \phi_i - \sum_{j=1}^{N_\theta} \cos \theta_j \right)^2 \right]. \quad (9)$$

Because of the identities  $\sin \theta = -\sin(\theta + \pi)$  and  $\cos \theta = -\cos(\theta + \pi)$ ,  $\mathcal{R}'$  reduces to the Rayleigh statistic  $\mathcal{R}$  except for the different ranges over which  $\theta_i$  and  $\phi_i$  are defined. In the limit of many detections over many periods,  $N_\phi \rightarrow N_\theta$  and  $\mathcal{R}'$  obeys exactly the same statistics as  $\mathcal{R}$  but with a more general null hypothesis.

One may search for periodicity either at a pre-determined frequency or by sweeping through parameter space. Here, we perform a coarse sweep, sampling periods from 5 to 40 ms in intervals of 1 ms. We choose a threshold value of 13.16 for  $\mathcal{R}'$ , which gives a 5% probability of a spurious detection. We then calculate the fraction of Monte Carlo realizations of signals computed at a given distance that exceed this threshold in at least one frequency. These fractions are our estimated probabilities of detecting high-frequency periodicity.

Figure 5 shows these detection probabilities as a function of supernova distance for both the IceCube and Super-K neutrino detectors. We estimate the detectability under both the optimistic assumption of no flavor mixing and the pessimistic assumption

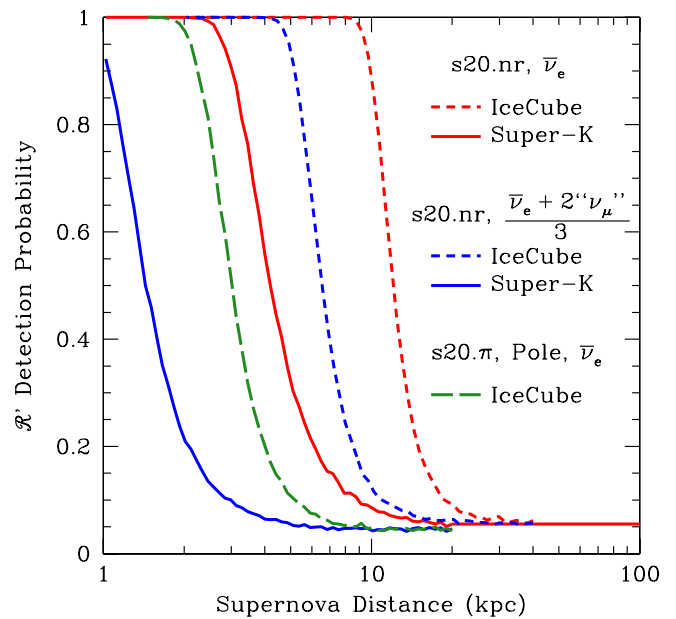


**Figure 5.** Probability of a  $2\sigma$  detection of at least one rapidly varying component of the neutrino luminosity using the modified Rayleigh test (Equation (9)) on Monte Carlo realizations of the estimated signals in  $\bar{\nu}_e$  and  $1/3\bar{\nu}_e + 2/3\bar{\nu}_\mu$  shown in Figure 4. Depending on the extent of neutrino mixing, rapid neutrino fluctuations in our nonrotating model may be detectable by IceCube as far away as  $\sim 10$  kpc. High-frequency fluctuations would be detectable by IceCube only within  $\sim 3$  kpc even under the optimistic assumption that no flavor mixing occurs.

(A color version of this figure is available in the online journal.)

that the flavors blend completely. The true signal will almost certainly lie somewhere in between, but will require a detailed calculation with a given mass hierarchy and mixing angle, which is beyond the scope of this paper. Even with the pessimistic assumption of complete flavor interchange, rapid fluctuations in our nonrotating model would be detectable by IceCube if the supernova were to occur within  $\sim 5$  kpc.

Figure 5 shows the distance at which *any* rapidly varying component may be detected. To gain physical insight into the nature of the shock oscillations, we would need a more detailed power spectrum of the high-frequency variation. Figure 6 shows the same detection probabilities as plotted for IceCube in Figure 5, but as a function of assumed period at four distances. A detailed measurement of the power spectrum of neutrino fluctuations, with statistically significant detections at several periods, would be possible for a supernova near the Galactic center, given the (optimistic) assumption of no flavor mixing.

## 6. THE EFFECTS OF ROTATION ON NEUTRINOS

Much of the previous discussion has focused on the consequences of convection, shock oscillations, and multi-angle neutrino transport. Our rapidly rotating model is fundamentally different in these respects. Convection near the equator is strongly inhibited by centrifugal support (see the discussion in Fryer & Heger 2000). As shown in Figures 19 and 21 of Ott et al. (2008), convective overturn tends to be confined to the polar regions where the centrifugal support is weaker, and strong shock oscillations do not begin to develop until about 400 ms after bounce. The rotating core evolves relatively smoothly, and is dominated spatially by quadrupole variations in the matter distribution and neutrino flux. The small-scale variations presented in Section 3 and shock oscillations explored in Section 4 are both strongly suppressed.

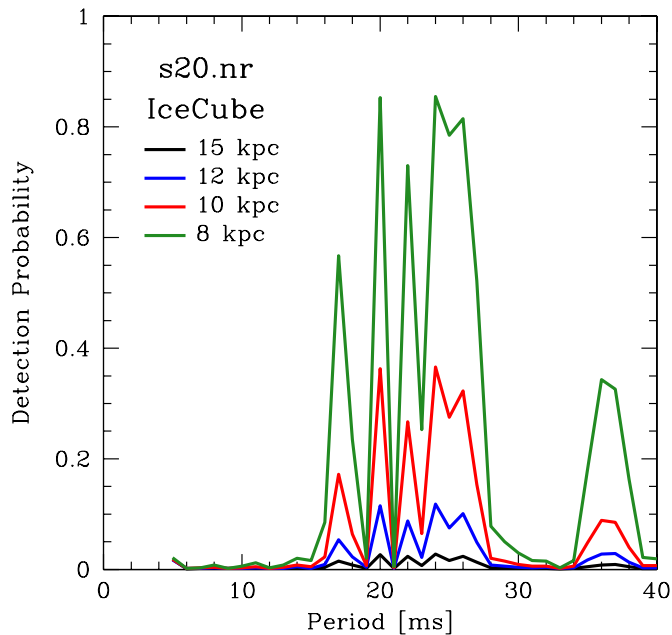


**Figure 6.** Probability of detecting high-frequency variation in the anti-electron neutrino luminosity with IceCube and the modified Rayleigh test (Equation (9)) at a given periodicity. In our nonrotating model, neglecting flavor oscillations, details of the SASI should be observable in neutrinos out to  $\sim 8$  kpc.

(A color version of this figure is available in the online journal.)

Rapid rotation creates centrifugal support and an oblate distribution of matter around the protoneutron star. At small radii, where the matter is optically thick, the radiation fields are similarly oblate. The neutrino distribution transitions to a prolate form beyond the oblate neutrinospheres (Kotake et al. 2003). Figure 7 shows this transition. We measure the prolateness or oblateness of the density and neutrino energy densities using the quadrupole coefficient of a spherical harmonic decomposition. Normalizing by the average value at (spherical) radius  $r$ , we define

$$\frac{\alpha_2(r)}{\alpha_0(r)} \equiv \frac{\oint d\Omega Y_2^0(\Omega) X(r)}{\oint d\Omega Y_0^0(\Omega) X(r)} \quad (10)$$

for a given quantity  $X$ .

The general forms of the matter density and neutrino fluxes, shown in Figure 7, are generic in rotating cores. The scale and extent of the matter oblateness are set by the rotation profile. As discussed in Section 2 of this paper and in Ott et al. (2008), rapid rotation in our model produces a relatively large quadrupole moment in the density and in the asymptotic neutrino fluxes. Our model rotates more rapidly than any presented in the previous studies of Janka & Mönchmeyer (1989), Walder et al. (2005), and Kotake et al. (2003). We now examine the effects of such rapid rotation, from the point of view of an observer measuring the neutrino flux at a single angle.

Asymmetries in neutrino flux naturally lead a randomly oriented observer to infer an incorrect luminosity. We explore and quantify this effect as a function of neutrino species and of time in our rapidly rotating model, comparing the inferred luminosity,  $4\pi r^2 F_\nu$ , to the actual neutrino luminosity,

$$L_\nu = \oint r^2 F_\nu d\Omega. \quad (11)$$

Here,  $r$  represents a radius sufficiently large that all neutrino species and energies are well into the free-streaming regime.

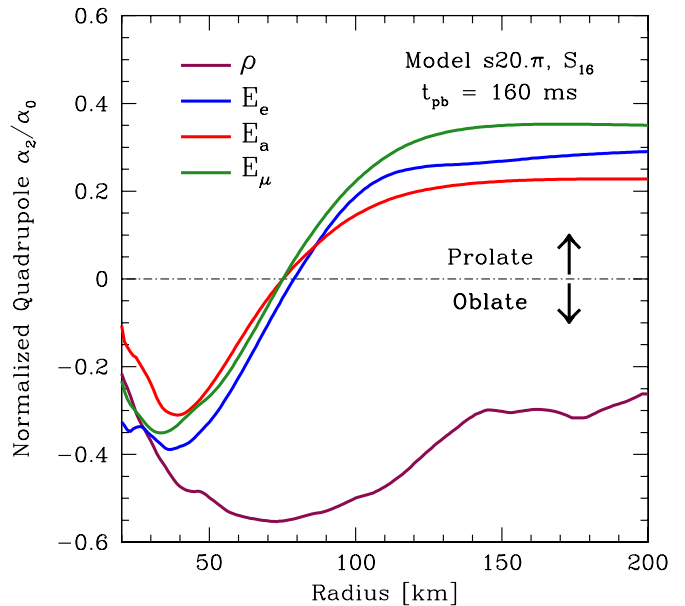


**Figure 7.** Normalized quadrupole moments (Equation (10)) of the neutrino energy densities and matter densities in our rapidly rotating model at 160 ms after bounce.  $E_e$ ,  $E_a$ , and  $E_\mu$  denote the total energy density in  $\nu_e$ ,  $\bar{\nu}_e$ , and “ $\nu_\mu$ ,” respectively. The centrifugally supported matter remains oblate throughout the computational domain. The radiation fields follow the matter in optically thick regions, but become prolate as they decouple, with neutrinos escaping more freely near the poles.

(A color version of this figure is available in the online journal.)

We use  $r = 150$  km for our calculations in order to satisfy this requirement, while minimizing the effects of  $S_n$  artifacts (Section 3.2).

In Section 6.1, we compute the angular distribution of neutrino flux and the probability distribution of inferred luminosities in our  $S_{16}$  snapshot at 160 ms after bounce. In Section 6.2, we show how these distributions evolve in time. Because of the limited angular resolution of our evolutionary calculation,  $S_n$  artifacts in the asymptotic fluxes become significant at late times. We remove this effect at the cost of angular resolution by integrating over each of the eight bands in polar angle.

### 6.1. Flux Asymmetries: Snapshots

In Figure 8, we present results for our 160 ms  $S_{16}$  rotating snapshot. The left panel shows the total neutrino energy flux in each species as a function of  $\mu \equiv \cos \theta$ . Large pole–equator flux asymmetries are present in all species, ranging from a factor of 2.1 in  $\bar{\nu}_e$  to a factor of 3.2 for “ $\nu_\mu$ .” This corresponds to an overestimate of the true luminosity by 100% ( $\nu_e$ ), 60% ( $\bar{\nu}_e$ ), or 110% (“ $\nu_\mu$ ”) at the poles, or an underestimate by 27% ( $\nu_e$ ), 23% ( $\bar{\nu}_e$ ), or 34% (“ $\nu_\mu$ ”) at the equator. These asymmetries are comparable to or slightly larger than those reported by Janka & Mönchmeyer (1989), who find as much as a factor of three, and Walder et al. (2005), who reach a factor of 2.5. This is likely due to the extreme rotation of our model, which is higher than in any of the models presented by Walder et al. (2005). In contrast, pole–equator asymmetries are  $\lesssim 4\%$  in the nonrotating model even though it manifests strong convective plumes and eddies (see Section 3).

In the right panel of Figure 8, we convert the angular distribution of neutrino flux into a probability distribution by assuming the observer to be randomly oriented with respect to the axis of rotation. Such an observer would have a 34% chance of being within 20% of the actual luminosity in  $\nu_e$ , a 54%

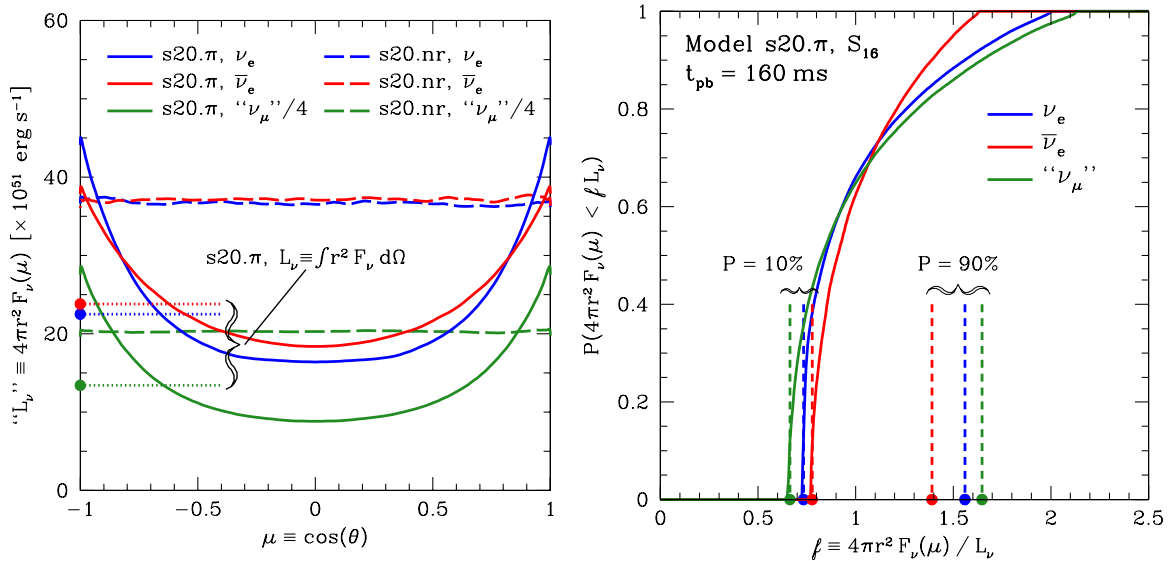


**Figure 8.** Left panel: spheritized neutrino luminosities ( $4\pi r^2 F_\nu$ ) as a function of viewing angle for the  $S_{16}$  snapshots. The short dashed lines indicate the true luminosities (integrated over  $4\pi$  steradians) for the rapidly rotating model. Fluxes are calculated at 150 km, after they have nearly reached their asymptotic values, but before  $S_n$  banding becomes noticeable. Right panel: probability of inferring less than a given fraction of the true neutrino luminosity in our rapidly rotating snapshot. Even at 160 ms after bounce, there is a 14% chance of overestimating the luminosity in “ $\nu_\mu$ ” by at least 50% and a 28% chance of underestimating it by at least 30%. This is especially important if flavor oscillations mix “ $\nu_\mu$ ” with the more uniform (and more easily detectable)  $\nu_e$  and  $\bar{\nu}_e$ . (A color version of this figure is available in the online journal.)

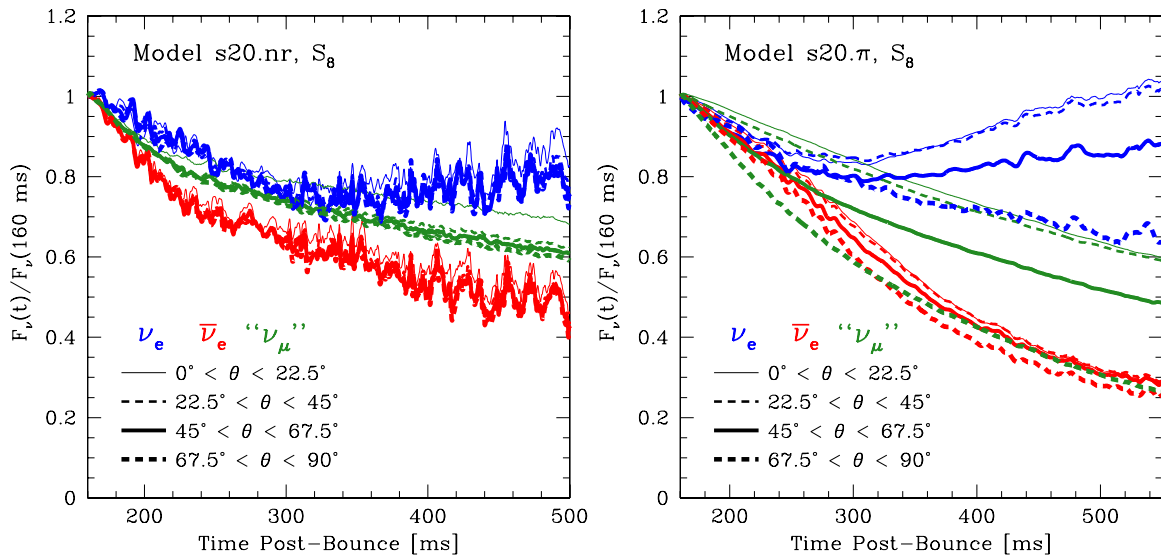


**Figure 9.** Light curves of the nonrotating (left panel) and rapidly rotating (right panel) models over four ranges of polar viewing angles from  $0^\circ$  to  $90^\circ$ , normalized to 160 ms after bounce. The angular ranges integrate over  $S_n$  artifacts, and we use line thicknesses proportional to the solid angle subtended. Because the flux is nearly symmetric about the equator, we only show viewing angles for the northern hemisphere. The nonrotating model has orientation effects of  $\lesssim 10\%$ , comparable in magnitude to temporal fluctuations. The rapidly rotating model has a nearly constant asymmetry in  $\bar{\nu}_e$  flux, but its “ $\nu_\mu$ ” light curve declines twice as fast near the equator as it does near the north pole. The  $\nu_e$  flux decreases by  $\sim 35\%$  near the equator, while actually *increasing* near a pole. Because of the differences between light curves of the various species, flavor oscillations could have a large effect on the shape of observed light curves. (A color version of this figure is available in the online journal.)

chance in  $\bar{\nu}_e$ , and a 28% chance in “ $\nu_\mu$ .” These distributions have significant tails, particularly for “ $\nu_\mu$ ’s” for which there is a 14% chance of observing at least 1.5 times the mean flux and a 2.3% chance of observing at least twice the mean.

All of these calculations neglect neutrino flavor oscillations. Should the species mix, anti-electron neutrinos detectable in IceCube and Super-K could blend with mu and tau antineutrinos, increasing the observable asymmetry in  $\bar{\nu}_e$ . Flavor oscillations would thus increase the uncertainty in inferring the true neutrino luminosity.

## 6.2. Light-curve Asymmetries

A core-collapse supernova’s neutrino light curve is a probe of the physical processes deep within the collapsed core. There is a burst of  $\nu_e$  emission as the shock wave reaches the electron neutrinospheres (Burrows & Mazurek 1983). The early postbounce phase is powered by accretion onto the core, while much of the total energy emerges during the tens of seconds duration of the protoneutron star phase (Burrows & Lattimer 1986). A rapidly rotating supernova will have a light

curve strongly dependent on viewing angle, particularly during the accretion-powered phase a few hundred milliseconds after bounce. In this section, we compute the light-curve shape as a function of viewing angle in both our nonrotating and our rapidly rotating models.

Unfortunately, our evolutionary calculations lack the polar angle resolution to accurately calculate the angular distribution of neutrino fluxes at large radius. As the neutrinospheres sink and optical depths decrease at fixed radius,  $S_n$  banding becomes significant at smaller radii. We remove these artifacts at the cost of angular resolution, by calculating average fluxes over angular wedges of  $22.5^\circ$  (an  $S_n$  band, or one-eighth of a hemisphere). We may still measure the evolution of the pole–equator asymmetry by choosing one band near the pole and a second near the equator. Because the flux is nearly symmetric with respect to the equator (see Figure 18 of Ott et al. 2008), we only show results for polar viewing angles in the range  $0^\circ < \theta < 90^\circ$ . We normalize all observed fluxes to their values at 160 ms after bounce to show evolutionary differences. These are arguably more significant than the total inferred power, as they are insensitive to uncertainties in distance.

We show our results in Figure 9. The nonrotating model (left panel) shows little variation in its light curve with angle. In this case, variations with angle are  $\lesssim 10\%$ , comparable to or lower in magnitude than rapid temporal fluctuations. However, orientation effects dominate the light curves of the rapidly rotating model (right panel). The shape of the light curve shows little variation with angle in  $\bar{\nu}_e$ , but declines twice as much in thermal “ $\nu_\mu$ ’s” near the equator as near a pole. The flux in  $\nu_e$ , while declining by  $\sim 35\%$  near the equator, actually *increases* for an observer near a pole. Because water Cherenkov detectors such as IceCube and Super-K are primarily sensitive to  $\bar{\nu}_e$ , the degree to which the less uniform “ $\nu_\mu$ ” mix with  $\bar{\nu}_e$  will determine not only the observed luminosity, but also the shape of the observed neutrino light curve.

## 7. CONCLUSIONS

We have presented new results from the only two-dimensional core-collapse calculations with full multi-angle neutrino transport. We have computed the spatial distributions of matter and radiation fields, finding that the radiation fields are more uniform than matter fields throughout the crucial gain region. This is both a result of the location of the decoupling region (primarily beneath the base of the convective region) and due to the multi-angle character of the specific intensity, so that the radiation at a point is an integral over many sources at depth. This latter effect can only be properly captured by full multi-angle neutrino transport. Our calculations therefore provide an important calibration test of methods, like the “ray-by-ray” approach, that do not naturally handle lateral transport.

We have measured the relationship of the radiation fields to the large-scale, low-order mode shock oscillations, the most striking feature of two-dimensional core-collapse simulations. This provides an important way to connect observable fluctuations in the neutrino luminosity to the otherwise unobservable hydrodynamics around the collapsed core. We have also calculated the phasing of the dipole moments of hydrodynamic quantities with the shock radius, demonstrating both the temporal structure of the oscillations and their variation with depth.

Following earlier work by Marek et al. (2009) and Lund et al. (2010), we have estimated the detectability of temporal fluctuations in the neutrino luminosity by the current water Cherenkov detectors IceCube and Super-K. We use a novel variant of the

Rayleigh test for periodicity. With our modification, the test takes its null hypothesis to be any smoothly varying signal, not simply a constant signal. This modified Rayleigh test applies to a wider range of problems in which a periodic, rapidly varying component is superimposed on *any* secularly changing signal. We find that neglecting neutrino flavor oscillations, we expect to measure a reasonably detailed power spectrum with IceCube for our nonrotating model within  $\sim 8$  kpc. Under these same (likely optimistic) assumptions, Super-K would be able to detect rapid fluctuations out to a distance of only  $\sim 3$  kpc. Given the pessimistic assumption that all neutrino species mix uniformly, rapid fluctuations in our nonrotating model would be detectable in IceCube out to  $\sim 5$  kpc, but a detailed power spectrum would probably lie beyond the capabilities of current detectors. The true signal will almost certainly lie somewhere in between these extremes of no and total mixing. This raises interesting prospects for the next Galactic supernova, if the low-mode shock oscillations in our nonrotating model are comparable in magnitude to those found in nature. Additional and complementary information could be gained by the observation of gravitational waves that carry with them the imprint of multi-dimensional dynamics in core and post-shock region (Ott 2009; Murphy et al. 2009; Marek et al. 2009; Yakunin et al. 2010).

We also analyzed the angular distribution of radiation in our rapidly rotating model and its effects on the luminosities and light curves measured by randomly oriented observers. We find pole–equator asymmetries at least as large as Janka & Mönchmeyer (1989), and larger than any of the models studied by Walder et al. (2005), though ours also rotates somewhat faster. The asymmetries are strongly dependent on neutrino species, with “ $\nu_\mu$ ” showing the greatest asymmetry (a factor of  $\sim 3$  at 160 ms after bounce) and  $\bar{\nu}_e$  the least (a factor of  $\sim 2$ ). The light curves of our rapidly rotating model are also strong functions of species and of angle, and again, the “ $\nu_\mu$ ” show the greatest asymmetry and  $\bar{\nu}_e$  the least. By 550 ms after bounce, the pole–equator asymmetry remains a factor of  $\sim 2$  in  $\bar{\nu}_e$ , but has grown to  $\sim 6$  in “ $\nu_\mu$ .” The asymmetry in any observed signal thus depends strongly on the degree of neutrino flavor mixing. Because of the strong dependence of the light curves on angle, a randomly oriented observer could face considerable uncertainty in the timescale, not simply the magnitude, of the neutrino emission.

By treating the neutrino–matter coupling accurately in the crucial gain region, our calculations have enabled a detailed study of the spatial and temporal character of the radiation fields. These will enable the calibration of less accurate (and much less expensive) radiative transfer techniques. They also demonstrate the strikingly uniform character of radiation in the gain region. Our estimates of the detectable features of our models also suggest that the next Galactic supernova may offer an observational test of the dipolar shock oscillations common to two-dimensional core-collapse simulations, and highlight the uncertainty associated with neutrino measurements of a rapidly rotating core.

The authors acknowledge fruitful ongoing and past collaborations with, conversations with, or input from Jason Nordhaus, Emmanouela Rantsiou, and Evan O’Connor. This material is based upon work supported under a National Science Foundation Graduate Research Fellowship to T.D.B. A.B. is supported by the Scientific Discovery through Advanced Computing (SciDAC) program of the DOE, under grant number DE-FG02-08ER41544, the NSF under the subaward number ND201387

to the Joint Institute for Nuclear Astrophysics (JINA, NSF PHY-0822648), and the NSF PetaApps program, under award OCI-0905046 via a subaward number 44592 from Louisiana State University to Princeton University. C.D.O. is partially supported by the NSF under grant numbers AST-0855535 and OCI-0905046. Computational resources were provided by the TIGRESS high-performance computer center at Princeton University, which is jointly supported by the Princeton Institute for Computational Science and Engineering (PICSciE) and the Princeton University Office of Information Technology. Other computational resources used include the NSF TeraGrid under award TG-PHY100033, the Caltech NSF MRI-R<sup>2</sup> cluster Zwicky (PHY-1057238), and the Louisiana Optical Network Infrastructure compute clusters under award Ioni\_numrel05.

## REFERENCES

- Bethe, H. A. 1990, *Rev. Mod. Phys.*, **62**, 801
- Bethe, H. A., & Wilson, J. R. 1985, *ApJ*, **295**, 14
- Blondin, J. M., Mezzacappa, A., & DeMarino, C. 2003, *ApJ*, **584**, 971
- Bruenn, S. W., Mezzacappa, A., Hix, W. R., Blondin, J. M., Marronetti, P., Messer, O. E. B., Dirk, C. J., & Yoshida, S. 2010, arXiv:1002.4914
- Buras, R., Rampp, M., Janka, H., & Kifonidis, K. 2006, *A&A*, **447**, 1049
- Burrows, A., Dessart, L., & Livne, E. 2007, in AIP Conf. Proc. 937, *Supernova 1987A: 20 Years After: Supernovae and Gamma-Ray Bursters*, ed. S. Immler, K. Weiler, & R. McCray (Melville, NY: AIP), 370
- Burrows, A., Hayes, J., & Fryxell, B. A. 1995, *ApJ*, **450**, 830
- Burrows, A., & Lattimer, J. M. 1986, *ApJ*, **307**, 178
- Burrows, A., Livne, E., Dessart, L., Ott, C. D., & Murphy, J. 2007, *ApJ*, **655**, 416
- Burrows, A., & Mazurek, T. L. 1983, *Nature*, **301**, 315
- Castor, J. I. 2004, *Radiation Hydrodynamics* (Cambridge: Cambridge Univ. Press)
- Colgate, S. A., & White, R. H. 1966, *ApJ*, **143**, 626
- Demorest, P. B., Pennucci, T., Ransom, S. M., Roberts, M. S. E., & Hessels, J. W. T. 2010, *Nature*, **467**, 1081
- Emmering, R. T., & Chevalier, R. A. 1989, *ApJ*, **345**, 931
- Faucher-Giguère, C., & Kaspi, V. M. 2006, *ApJ*, **643**, 332
- Fernández, R. 2010, *ApJ*, **725**, 1563
- Foglizzo, T., Galletti, P., Scheck, L., & Janka, H. 2007, *ApJ*, **654**, 1006
- Foglizzo, T., & Tagger, M. 2000, *A&A*, **363**, 174
- Fryer, C. L., & Heger, A. 2000, *ApJ*, **541**, 1033
- Fryer, C. L., & Warren, M. S. 2002, *ApJ*, **574**, L65
- Fryer, C. L., & Warren, M. S. 2004, *ApJ*, **601**, 391
- Fryer, C. L., & Young, P. A. 2007, *ApJ*, **659**, 1438
- Heger, A., Woosley, S. E., & Spruit, H. C. 2005, *ApJ*, **626**, 350
- Herant, M., Benz, W., Hix, W. R., Fryer, C. L., & Colgate, S. A. 1994, *ApJ*, **435**, 339
- Ikeda, M., et al. 2007, *ApJ*, **669**, 519
- Iwakami, W., Kotake, K., Ohnishi, N., Yamada, S., & Sawada, K. 2008, *ApJ*, **678**, 1207
- Janka, H., Langanke, K., Marek, A., Martínez-Pinedo, G., & Müller, B. 2007, *Phys. Rep.*, **442**, 38
- Janka, H., & Mönchmeyer, R. 1989, *A&A*, **209**, L5
- Janka, H., & Mueller, E. 1996, *A&A*, **306**, 167
- Kitaura, F. S., Janka, H., & Hillebrandt, W. 2006, *A&A*, **450**, 345
- Kotake, K., Yamada, S., & Sato, K. 2003, *ApJ*, **595**, 304
- Kowarik, T., Griesel, T., & Pięgsa, A. (The Icecube Collaboration) 2009, Proc. 31st ICRC (Lodz), in press (arXiv:0908.0441)
- Leahy, D. A., Elsner, R. F., & Weisskopf, M. C. 1983, *ApJ*, **272**, 256
- Liebendörfer, M., Mezzacappa, A., Thielemann, F., Messer, O. E., Hix, W. R., & Bruenn, S. W. 2001, *Phys. Rev. D*, **63**, 103007
- Liebendörfer, M., Rampp, M., Janka, H., & Mezzacappa, A. 2005, *ApJ*, **620**, 840
- Livne, E., Burrows, A., Walder, R., Lichtenstadt, I., & Thompson, T. A. 2004, *ApJ*, **609**, 277
- Lund, T., Marek, A., Lunardini, C., Janka, H., & Raffelt, G. 2010, *Phys. Rev. D*, **82**, 063007
- Maeder, A., & Meynet, G. 2000, *ARA&A*, **38**, 143
- Marek, A., & Janka, H. 2009, *ApJ*, **694**, 664
- Marek, A., Janka, H., & Müller, E. 2009, *A&A*, **496**, 475
- Murphy, J. W., & Burrows, A. 2008, *ApJ*, **688**, 1159
- Murphy, J. W., Ott, C. D., & Burrows, A. 2009, *ApJ*, **707**, 1173
- Nordhaus, J., Burrows, A., Almgren, A., & Bell, J. 2010, *ApJ*, **720**, 694
- Ott, C. D. 2009, *Class. Quantum Grav.*, **26**, 204015
- Ott, C. D., Burrows, A., Dessart, L., & Livne, E. 2008, *ApJ*, **685**, 1069
- Ott, C. D., Burrows, A., Thompson, T. A., Livne, E., & Walder, R. 2006, *ApJS*, **164**, 130
- Rampp, M., & Janka, H. 2000, *ApJ*, **539**, L33
- Scheck, L., Janka, H., Foglizzo, T., & Kifonidis, K. 2008, *A&A*, **477**, 931
- Shen, H., Toki, H., Oyamatsu, K., & Sumiyoshi, K. 1998a, *Nucl. Phys. A*, **637**, 435
- Shen, H., Toki, H., Oyamatsu, K., & Sumiyoshi, K. 1998b, *Prog. Theor. Phys.*, **100**, 1013
- Shlomo, S., Kolomietz, V. M., & Colò, G. 2006, *Eur. Phys. J. A*, **30**, 23
- Thompson, T. A., Burrows, A., & Pinto, P. A. 2003, *ApJ*, **592**, 434
- Walder, R., Burrows, A., Ott, C. D., Livne, E., Lichtenstadt, I., & Jarrah, M. 2005, *ApJ*, **626**, 317
- Woosley, S. E. 1993, *ApJ*, **405**, 273
- Woosley, S. E., Heger, A., & Weaver, T. A. 2002, *Rev. Mod. Phys.*, **74**, 1015
- Yakunin, K. N., et al. 2010, *Class. Quantum Grav.*, **27**, 194005
- Yamasaki, T., & Foglizzo, T. 2008, *ApJ*, **679**, 607